



# Anodizing by Electrochemical Oxidation (ECO) of the Laser Powder Bed Fusion-processed A357 aluminium alloy: microstructural characterization and dry sliding behaviour

Luca Lorenzetti<sup>1</sup> · Lavinia Tonelli<sup>1</sup> · Iuri Boromei<sup>1</sup> · Lorella Ceschini<sup>1</sup> · Pavel Shashkov<sup>2</sup> · Carla Martini<sup>1</sup>

Received: 4 February 2022 / Accepted: 6 October 2022  
© The Author(s) 2022

## Abstract

Considering the increasing interest for Al alloys in the packaging industry, where component lightweighting allows higher process efficiency, as well as the increasing use of additively manufactured parts, which may not show a satisfactory tribological behaviour in the as-built condition, anodising by Electrochemical Oxidation (ECO) and Plasma Electrolytic Oxidation (PEO) was applied to as-built A357 (AlSi7Mg0.6) produced by Laser Powder Bed Fusion (LPBF). ECO allowed to compensate surface and surface-connected defects in LPBF A357 and produced a thicker, less-defective anodic oxide than PEO, providing higher wear resistance whilst maintaining a lower Coefficient of Friction (COF) in dry sliding tests against 100Cr6 steel. Polishing before ECO only resulted in negligible friction and wear improvements, even if it improved the compactness of the anodic oxide.

**Keywords** Laser Powder Bed Fusion · Aluminium alloys · Microstructure · Surface roughness · Anodising · Sliding wear

## 1 Introduction

Al alloys are increasingly used in the packaging industry, where component lightweighting allows higher process efficiency. However, when involved in sliding contacts, these alloys display low resistance to adhesion and abrasion [1]. Moreover, Al alloys manufactured by additive processes, such as Laser Powder Bed Fusion (LPBF), may not show a satisfactory behaviour in the as-built condition due to surface and bulk defects, such as balling, lack-of-fusion zones, spatters, partially melted powders, and porosities, which can affect surface quality as well as mechanical and tribological properties [2]. Therefore, surface modification may contribute to improve the tribological behaviour of additively manufactured Al alloys, with the aim of extending their use in all those applications that may benefit from lightweighting. Among Al alloys, this work focuses on hypoeutectic A357

(AlSi7Mg0.6), characterised by excellent resistance to hot tearing, narrow solidification range (close to 55 °C), good fluidity, and weldability, making it appropriate for LPBF as well as for conventional casting processes [3].

For a long time, the most popular surface engineering technique applied to overcome these issues has been Hard Anodising (HA), that improves both tribological and corrosion properties. However, Si particles in Al–Si alloys anodize at a reduced rate compared with the aluminium matrix [4] and both Si particles and AlFeSi intermetallic compounds, usually present in Al–Si alloys, are detrimental for the growth of the anodic oxide [5]. Moreover, Si particles may shield the Al-rich phase trapped beneath or between Si and prevent it from oxidation [6]. In a recent study, HA by galvanostatic anodising at room temperature in 3 M H<sub>2</sub>SO<sub>4</sub> at 10 mA/cm<sup>2</sup> was applied to LPBF-fabricated AlSi10Mg, proving that its very fine microstructure, promoted by the high cooling rate typical of the LPBF process (i.e., 10<sup>5</sup>–10<sup>6</sup> K/s), positively affects the compactness of the anodic oxide by comparison to the corresponding cast alloy [7]. The ultra-fine network of eutectic Si improves the uniformity and nanoscale roughness of the oxide layer in comparison to conventional as-cast alloy, leading to a more continuous protective coating, even though with lower growth rate and oxide thickness. When comparing the response of

✉ Luca Lorenzetti  
luca.lorenzetti5@unibo.it

<sup>1</sup> Department of Industrial Engineering, University of Bologna, Viale Risorgimento 4, 40136 Bologna, Italy

<sup>2</sup> Cambridge Nanolitic Ltd, 3b Homefield Road, Haverhill CB9 8QP, Suffolk, UK

LPBF-AlSi7Mg0.6, AlSi10Mg, and AlSi12 in the as-built condition to galvanostatic anodising in H<sub>2</sub>SO<sub>4</sub>, a tendency towards the growth of slightly thinner anodic oxide layers with increasing Si content in the alloys was observed, due to the increased thickness and connectivity of the Si network [8].

In the last decades, Plasma Electrolytic Oxidation (PEO) has been proposed as an alternative to HA. PEO is an electrochemical conversion treatment based on the growth of the anodic oxide at potentials exceeding the breakdown voltage of the dielectric film. In these conditions, a controlled micro-arc discharge regime favours the growth of thick, hard, adherent, and wear-resistant layers [9]. As opposed to HA that takes place in a concentrated acidic solution, PEO processes are carried out in dilute alkaline electrolytic baths and a higher tolerance than HA to alloying elements, such as Si and Cu, has been widely documented [10], making PEO more suitable for Al–Si alloys. Nevertheless, PEO layers display an intrinsically heterogeneous microstructure with micropores and cracks, mostly in the external (so-called “technological”) layer, which can lead to micro-cracking and coating removal in the form of flakes during tribological contacts [11]. Moreover, the characteristic high roughness of these coatings leads to high friction against steel counterparts in dry sliding conditions [12].

With the aim of limiting the drawbacks of PEO, an enhanced anodising process called ECO (Electrochemical Oxidation) has been recently developed (UK Patent GB2497063, Cambridge Nanolitic Ltd). ECO derives from PEO, but uses bipolar pulsed DC sources, avoiding disruptive plasma discharge effects and providing dense and compact coatings. The formation of an oxide layer with a finer nanopore structure is promoted by: (1) using short (micro-seconds) electrical pulses with trapezoidal shape, to reduce the electrical current peaks during pulse switching, (2) maintaining cathodic current at a level that secures cathodic etching, and (3) avoiding breakdown discharge and improving ions and charge transfer to the oxidation zone. ECO coatings have already found application in textile, packaging, and

automotive industries, but their microstructural and tribological properties are still under investigation. A comparison of the tribological behaviour of HA-, PEO-, and ECO-treated wrought AA6082-T5 has been recently published [13], but the ECO treatment has never been applied, until now, to LPBF AlSiMg alloys. On the other hand, only a few works report on the application of PEO to LPBF AlSiMg alloys. In particular, Pezzato et al. [14] discussed the influence of microstructure and porosities on the corrosion behaviour of PEO-treated AlSi10Mg, whilst Rogov et al. [15] discussed the electrochemical behaviour of AlSi12 (either cast or LPBF) during AC-PEO in silicate alkaline electrolyte. Hence, there is a substantial lack of data about the application of PEO and ECO processes on LPBF A357 alloy, especially regarding the influence of these treatments on its tribological behaviour.

Based on the above considerations, the present work focuses on the microstructure characterisation and tribological behaviour of ECO and PEO layers grown on as-built LPBF A357, fabricated from the same batch of powder by two different sets of process parameters aimed at: (i) maximum productivity and (ii) microstructure improvement. Sand-cast A357 alloy, subjected to hot-isostatic pressing and T6 heat treatment, was used as a benchmark in the case of the ECO process.

## 2 Materials and methods

### 2.1 LPBF sample production

Small bars of A357 (5 × 5 × 70 mm<sup>3</sup>) were produced by LPBF starting from gas-atomised powder provided by LPW technology (currently LPW Carpenter Additive, Carpenter Technology Corporation, USA), whose composition is reported in Table 1. The powder was dried before the LPBF process at 60 °C for 3 h to reduce moisture. All the samples were built in a single batch using an LPBF machine

**Table 1** Chemical composition of A357 samples (wt.%): comparison of experimental results (GD-OES) with nominal composition of feedstock powder [16] and A357 alloy [17].

	Elements (wt %)							
	Al	Si	Mg	Fe	Ti	Zn	Mn	Others
Powder	Bal	6.90	0.55	0.10	0.09	<0.01	<0.01	<0.15
P	Bal	7.02	0.54	0.09	0.15	0.08	<0.01	<0.03
M	Bal	6.98	0.57	0.09	0.15	0.08	<0.01	<0.03
C	Bal	6.88	0.59	0.07	0.16	0.09	0.01	<0.04
<i>Nominal</i>	<i>Bal</i>	<i>6.50–7.50</i>	<i>0.45–0.70</i>	<i>0.12</i>	<i>0.04–0.20</i>	<i>0.05</i>	<i>0.05</i>	<i>max 0.10</i>

Italic values indicate the nominal composition of feedstock powder

P, LPBF samples printed in conditions for maximum productivity; M, LPBF samples printed in conditions for microstructure improvement; C, sand-cast + HIP + T6

(MYSINT100 RM manufactured by SISMA) equipped with 200 W laser source with a nominal spot diameter of 55  $\mu\text{m}$ . The LPBF process was carried out in a  $\text{N}_2$  environment with a residual oxygen content of 0.1 vol%, using vertical building direction (i.e., perpendicular to the building platform), no platform pre-heating and conical supports.

Laser power was set at 175 W and, as disclosed in Table 2, scanning strategy and process parameters were set as follows: (i) printing in conditions of maximum productivity (i.e., P series); (ii) printing under improved microstructure conditions (i.e., M series), leading to a reduced porosity content [18]. For the production of both P and M series, skywriting was enabled.

The chemical composition of the LPBF samples was checked by Glow Discharge Optical Emission Spectroscopy (GD-OES, Spectruma Analytik GDA 650) with a Grimm-style glow discharge lamp in DC mode. The analysed area in each measurement was about 5  $\text{mm}^2$ , corresponding to the internal area of the tubular anode (2.5 mm diameter). Results are reported in Table 1 and showed that LPBF samples retained the powder composition. In the same table, also the composition of the conventional sand-cast alloy used as benchmark and subjected to hot-isostatic pressing and T6 treatment (henceforward labelled “C”) is compared. All the investigated compositions were comparable and coherent with nominal requirements for the A357 alloy.

With the aim of evaluating the improvement in the tribological behaviour of LPBF A357 alloy induced by anodising only, no heat treatment was applied. Therefore, all the LPBF substrates were investigated in the as-built condition.

## 2.2 PEO and ECO treatments

The main parameters of ECO and PEO anodising treatments, carried out in an industrial environment, are summarised and compared in Table 3. The main differences between the treatments are related to current density, coating mode control, and electrolyte. In ECO, an optimal ratio between anodic and cathodic pulse currents allowed to produce a low-discharge oxidation effect.

The present work focuses on: (i) comparing ECO and PEO layers grown on LPBF M and P samples, and (ii) comparing the ECO layers grown on LPBF and cast substrates. Therefore, whilst the ECO treatment was applied on all the investigated samples, PEO was applied only to LPBF samples. As already mentioned, LPBF samples were anodised in the as-built condition, meaning that no post-process polishing or heat treatments were applied before anodising. However, only for the ECO treatment, also the effect of a standardised procedure, based on the use of a given polishing medium (i.e., an 800 grit emery paper) on surfaces with a variable roughness, was investigated. For this reason, the ECO layers which underwent this procedure were henceforward called “pre-polished”, to highlight that polishing was carried out before anodising. After all the PEO and ECO treatments, no surface finishing treatment was applied, so as to simulate the situation in which grinding or polishing at the end of the anodising treatment was not applicable due to complex part geometry.

**Table 2** LPBF-process parameters applied for the production of the A357 samples

Series	Power [W]	Scanning strategy	Hatch spacing [mm]	Layer thickness [mm]	Scanning Speed [mm/s]	Energy density [ $\text{J}/\text{mm}^3$ ]
P	175	4 × 4 $\text{mm}^2$ chessboard With 45° rotation between layers	0.12	0.02	1400	52.08
M	175	3 × 3 $\text{mm}^2$ chessboard With 45° rotation between layers	0.08	0.02	500	218.75

**Table 3** Main parameters of the anodising treatments

Process	Voltage/Current density Discharge effect	Coating mode control	Electrolyte	Process tank temperature	Electric equipment and conditions
Electro-chemical oxidation (ECO)	100–600 V/ 40–150 mA/ $\text{cm}^2$ Low-discharge oxidation	Potentiostatic for anodic pulse; galvanostatic for cathodic pulses	Colloidal alkaline phosphate solution (KOH, $\text{Na}_4\text{P}_2\text{O}_7$ , $\text{Al}(\text{OH})_3$ , nanopowder $\text{Al}_2\text{O}_3$ )	20–25 °C	Pulsed bipolar current (PBC) power supply
Plasma electrolytic oxidation (PEO)	50–650 V/80–170 mA/ $\text{cm}^2$ Micro-discharge oxidation	Potentiostatic for anodic and cathodic pulses	Alkaline phosphate solution (KOH, NaF, $\text{Na}_4\text{P}_2\text{O}_7$ )	20–25 °C	Pulsed bipolar current (PBC) power supply

### 2.3 Microstructural and micro-mechanical characterisation

Microstructural characterisation of the A357 alloy, before and after the anodising treatments, was carried out on samples prepared following standard metallographic techniques and chemically etched using Keller's reagent (1 mL HF, 1.5 mL HCl, 2.5 mL HNO<sub>3</sub>, 95 mL H<sub>2</sub>O and 20 s immersion at room temperature). Microstructural observations were carried out by optical microscopy (Reichert MEF3) and Field Emission Gun Scanning Electron Microscope (FEG-SEM Tescan Mira 3). To further investigate the elemental distribution, Energy-Dispersive Spectroscopy (EDS) X-ray maps were measured on polished cross-sections (Bruker XFlash 630 M). Layers thickness measurements were carried out using the ImageJ software by averaging data obtained by at least 5 measurements at the same magnification.

Surface roughness was measured on the free surfaces of samples, before and after the ECO treatment, by stylus profilometry (Hommelwerke T2000, tip radius: 5 µm), using  $L_t = 12.5$  mm (i.e., evaluation length) and  $L_c = 2.5$  mm (i.e., sampling length) in accordance with ISO 4288 [19]. Moreover, to further investigate the topography of the anodised surfaces, FEG-SEM Alicona MeX 6.2.1 imaging software was employed, based on eucentric tilting of the specimens during FEG-SEM observation. Topographic measurements were made on areas of about 60,000 µm<sup>2</sup>, at tilt angles from 5 to 10°.

The density of samples was evaluated with an analytical balance (0.0001 g precision), according to the Archimedes principle [20] and using a reference full density value of 2.68 g cm<sup>-3</sup> [21].

The phase constitution of PEO and ECO layers was determined using X-Ray Diffraction (XRD) by a PANalytical Expert PRO X-ray diffractometer with Xcelerator detector and a Ni-filtered Cu-Kα radiation source ( $\lambda = 0.15405$  nm), operated at 40 kV and 30 mA. The  $I_{\alpha}/I_{\gamma}$  ratio was determined for  $\alpha$ - and  $\gamma$ -Al<sub>2</sub>O<sub>3</sub> in the oxide layers comparing the integrated diffraction intensities of the (113)<sub>α</sub> peak ( $2\theta = 43.4^\circ$ ) and the (400)<sub>γ</sub> peak ( $2\theta = 45.7^\circ$ ) [22, 23], determined by the X'Pert High-Score Plus software (PANalytical).

Progressive load scratch tests were also carried out on the anodic oxide layers, using a Revetest device (CSM Instruments) equipped with a Rockwell diamond indenter (spherical tip radius: 200 µm). Normal load increased from 1 to 100 N, with a linear speed rate of 10 mm min<sup>-1</sup> and a scratch length of 10 mm.

Micro-hardness tests were carried out on polished cross-sections of the anodised samples using a Knoop micro-hardness tester with a load of 100 g (HK<sub>0.1</sub>).

### 2.4 Dry sliding tests

Dry sliding tests were carried out by a flat-on-cylinder tribometer (block-on-ring contact geometry, ASTM G-77 [24]). In this configuration, stationary sliders (i.e., 5 × 5 × 70 mm<sup>3</sup> bars) slid against a rotating 100Cr6 (AISI 52100) bearing steel cylinder (diameter: 40 mm), heat treated to 62 HRC, and surface finished to  $R_a = 0.09 \pm 0.03$  µm.

All the investigated samples are summarised in Table 4. With the aim to assess the effect of the anodising treatment on the wear resistance of the alloys, tests were also carried out on bare sliders (identified by P, M and C).

Each test was carried out at ambient conditions of humidity and temperature (relative humidity ranging from 50 to 60%) at fixed sliding speed (0.3 m s<sup>-1</sup>) up to a sliding distance of 1000 m and with normal loads of 20, 40, and 60 N. At least two repetitions were carried out for each testing condition. The selected normal loads led to the Hertzian maximum contact pressures in Table 5, estimated according to [25]. Hertzian contact pressure was calculated considering elastic modulus and Poisson's ratio for the prevalent phases in anodic oxides, as determined by XRD. Friction force values were continuously recorded during each test as a function of sliding distance, using a bending load cell. Coefficient of Friction (COF) values were then averaged over the steady-state regime for each test, set at 200–1000 m range for each test repetition not inducing full coating failure. The maximum wear depth on the sliders and on the cylinder was determined at the end of each test by means of a stylus profilometer (Hommelwerke T2000, tip radius: 5 µm), measuring at least three profiles on each wear scar (one in the centre and two at the sides). The worn surfaces were characterised by SEM

**Table 4** Summary of anodised A357 samples for dry sliding tests

Samples	Substrate		
	Manufacturing	Heat treatment	Polishing before anodizing
P	LPBF	–	–
P-ECO	LPBF	–	–
P-ECO pre-polished	LPBF	–	Yes
P-PEO	LPBF	–	–
M	LPBF	–	–
M-ECO	LPBF	–	–
M-ECO pre-polished	LPBF	–	Yes
M-PEO	LPBF	–	–
C	Sand cast	HIP+ T6	–
C-ECO	Sand cast	HIP+ T6	Yes

**Table 5** Maximum and mean Hertzian contact pressures on the anodised A357 alloy as a function of normal load (dry sliding against AISI 52100 bearing steel)

	Contact pressures, MPa					
	20 N		40 N		60 N	
	$P_{max}$	$P_{mean}$	$P_{max}$	$P_{mean}$	$P_{max}$	$P_{mean}$
P-ECO	89	70	125	98	154	121
P-PEO	88	69	124	98	152	120
M-ECO	92	72	130	102	159	125
M-PEO	88	69	124	98	152	120
C-ECO	91	71	128	101	157	123

(Zeiss EVO 50) equipped with EDS (Oxford Instruments x-act) to identify the dominant wear mechanisms.

### 3 Results and discussion

#### 3.1 Microstructure of A357 substrate

The microstructure of the A357 substrates is reported in Fig. 1, in which the 3D representations of the microstructure of P (Fig. 1a), M (Fig. 1b), and C (Fig. 1c) are compared. This representation shows the microstructure along three main planes: i) XY, perpendicular to the build direction (BD) Z; (ii) XZ, parallel to BD (i.e., the longitudinal axis of the sliders) and corresponding to the surfaces used for the sliding tests (Fig. 1d); (iii) YZ.

The C alloy (Fig. 1c) was characterised by the typical solidification microstructure of Al–Si cast alloy, consisting of primary  $\alpha$ -Al dendrites (SDAS equal to about  $51.8 \pm 2.7 \mu\text{m}$ ) surrounded by modified eutectic Si (average size of Si particles of about 5–10  $\mu\text{m}$ ). C microstructure can be considered homogeneous along all the investigated sections. The LPBF alloy, on the other hand, was characterised by a microstructure strongly dependent on

process parameters (as demonstrated also by [26]), and on the investigated section. At the same magnification, considering the XY sections, P and M samples (Fig. 1a, b) showed the typical microstructure induced by the LPBF process, with overlapping ellipsoidal solidified melt pools reproducing the adopted scanning strategy. The same melt pools along the XZ sections were instead characterised by the typical semi-circular shape. The comparison of LPBF substrates showed a more porous microstructure for the alloy printed with conditions for maximum productivity P (Fig. 1a) than for microstructurally improved M samples (Fig. 1b), as also confirmed by the measured relative density (99% for M, 97.7% for P).

Furthermore, sub-surface defects, such as lacks of fusion, were detected in P samples (Fig. 2), presumably as a result of the large hatch spacing and high scanning velocity adopted. Such a detrimental feature was not observed for M samples due to the optimised building conditions.

FEG-SEM high-magnification micrographs of LPBF samples taken along the longitudinal XZ section (Fig. 3a–d) showed the typical cellular structure formed inside the melt pool. Such microstructure is characterised by sub-micrometric  $\alpha$ -Al cells, surrounded by an interconnected network of eutectic Si (average size about 0.1–0.2  $\mu\text{m}$ ). Conversely,

**Fig. 1** 3D reconstructions of the microstructure of the A357 samples: (a) as-built P (maximum productivity); (b) as-built M (improved microstructure); (c) C (sand-cast + HIP + T6). The surface used for tribological tests corresponds to the XZ plane (highlighted in blue in the scheme (d))

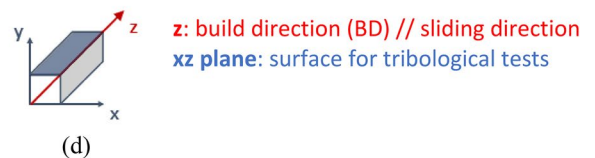
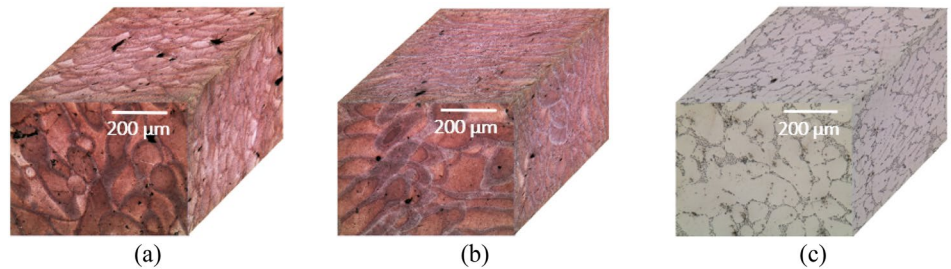


**Fig. 2** SEM images of *P* samples (polished cross-sections along XY plane), showing sub-surface defects due to lack of fusion at the contour layer edge: (a) general view and (b) high-magnification detail with spherical unmelted powders inside a cavity

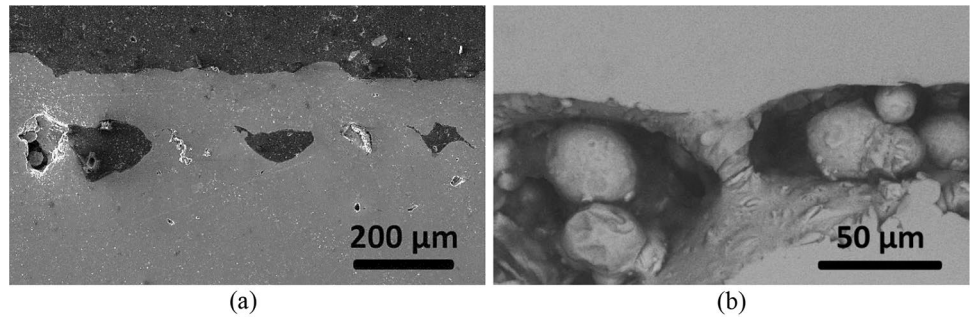
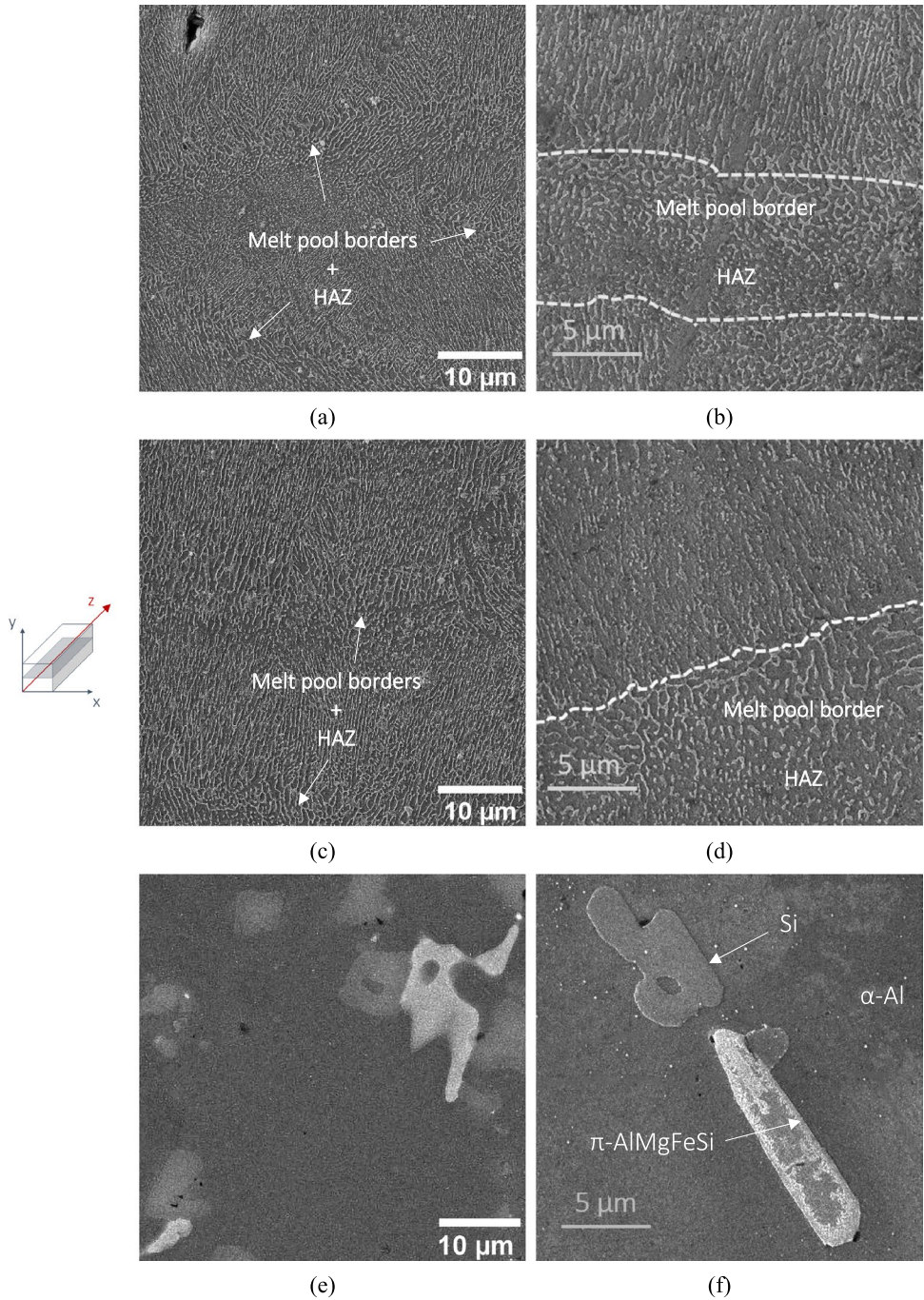


**Fig. 3** Low- and high-magnification FEG-SEM micrographs of the A357 substrates along XZ plane: (a, b) as-built P (maximum productivity); (c, d) as-built M (improved microstructure); (e, f) C (sand-cast + HIP + T6)



the C alloy showed a coarser microstructure, with large Si particles and Fe-rich intermetallic compounds (Fig. 3e, f). Therefore, in the LPBF microstructure, Si is more finely and uniformly distributed in the matrix than the cast alloy. In addition, Fe-rich intermetallic compounds were not detected by FEG-SEM analyses neither in M nor in P samples. The extremely fine microstructure of LPBF A357 was due to the high cooling rate occurring during the process, that led to the formation of a supersaturated and metastable solid solution, characterised by a peculiar microstructural fineness [27–30]. In general, the melt pool core showed a finer cellular structure than the surrounding area (melt pool borders and heat-affected zone, HAZ) [31]. M samples (Fig. 3c, d) showed a coarser cellular structure than P (Fig. 3a, b). This was likely due to the slower scanning speed (about 1/3 of that used for the P series) and reduced hatch spacing used leading to a higher value of the laser energy density for M (218.75 J/mm<sup>3</sup>) than for P (52.08 J/mm<sup>3</sup>). Therefore, the LPBF induced different thermal gradients between P and M series, and in M samples, larger areas of material were involved in the melting and re-heating processes, thus explaining the coarser and more interrupted microstructure.

### 3.2 PEO and ECO layers

#### 3.2.1 Surface roughness and morphology

The assessment of the surface quality of ECO and PEO layers was performed by comparing the linear and surface roughness values, reported in Table 6.

Roughness values were well correlated to the quality of the surfaces before treatment. The highest  $R_a$  and  $R_q$  values were, in fact, measured for P and M samples without pre-polishing, that were characterised by the poorest surface quality ( $R_a = 9 \div 16 \mu\text{m}$  and  $R_q = 13 \div 23 \mu\text{m}$  before treatment), typical of LPBF as-built surfaces [32]. However, it can be noticed that when applied to relatively smooth substrates as the C samples ( $R_a = 0.4 \pm 0.1 \mu\text{m}$  and  $R_q = 0.6 \pm 0.1 \mu\text{m}$  before treatment), ECO induced a roughness increase of

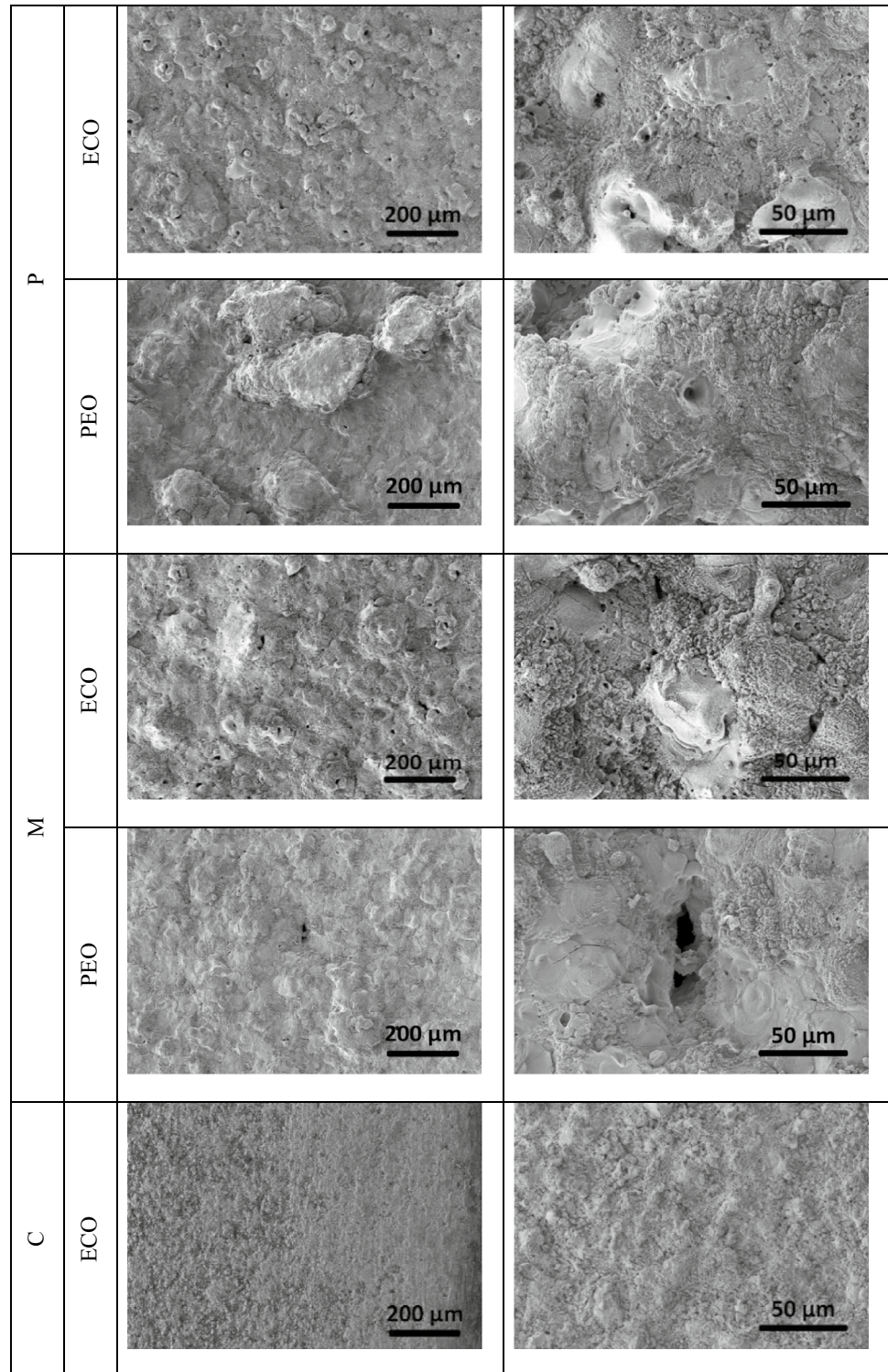
about three-to-four times (quantified as  $R_q$  ratio = 3.8, i.e.,  $R_q$  measured after anodising divided by  $R_q$  before anodising). On the other hand, when starting from the M and P as-built surfaces, characterised by a high surface roughness, the increase was negligible ( $R_q$  ratio =  $1 \div 1.1$ ). A similar trend was also observed for the PEO treatment, indicating that the localised discharge events occurring in both high-voltage anodising treatments produced surface morphologies with typical crater- and pancake-like features (shown in Fig. 4 and discussed in the following text). Therefore, both ECO and PEO treatment did not worsen the as-built surface quality. Moreover, the PEO treatment, which induces more intense micro-arc discharges [13], always led to slightly higher  $R_a$  and  $R_q$  values than the ECO treatment.

More detailed topographic analyses were carried out on ECO layers by comparing the surface parameters listed in Table 6. Results confirmed that the lowest  $S_a$  and  $S_q$  values were obtained on layers grown on the smoothest substrates (i.e., pre-polished LPBF and C substrates). In addition, linear ( $R_a$  and  $R_q$ ) and surface ( $S_a$  and  $S_q$ ) roughness parameters showed comparable values. The small differences observed using these two methods can be explained by the stochastic distribution of heights and the relatively small surface area that can be analysed by eucentric tilting (about 0.06 mm<sup>2</sup>). By focusing on the peak and valley distribution (assessed by the skewness  $S_{sk}$ ) and on the sharpness of the roughness profile (assessed by the kurtosis  $S_{ku}$  value), it can be also noticed that C-ECO layers showed the most homogeneous surface as proved by  $S_{sk} \approx 0$  (nearly Gaussian distribution of heights), and  $S_{ku} \approx 3$  (local maxima and minima were neither particularly wide nor too narrow [33]). Conversely, the ECO layers grown on unpolished LPBF substrates showed a less homogeneous surface, namely: (i) P series:  $S_{sk} < 0$  (valleys prevailing over peaks) and  $S_{ku} > 3$  (narrow peaks and valleys); (ii) M series:  $S_{sk} > 0$  (peaks prevailing over valleys) and again  $S_{ku} \geq 3$ . Pre-polishing of LPBF-fabricated substrates led to ECO layers with decreased  $S_{sk}$ , thus a prevalence of local minima (i.e., valleys), and increased  $S_{ku}$ , indicating that valleys became narrower.

**Table 6** Linear ( $R_a$  and  $R_q$ ) and surface roughness parameters [ $S_a$ ,  $S_q$ , skewness ( $S_{sk}$ ) and kurtosis ( $S_{ku}$ )] measured after anodising treatment, together with average thickness values and critical loads for adhesive failure ( $L_{c3}$ , scratch testing) of anodic oxides

	Surface roughness						Thickness ( $\mu\text{m}$ )	$L_{c3}$ (N)
	$R_a$ ( $\mu\text{m}$ )	$R_q$ ( $\mu\text{m}$ )	$S_a$ ( $\mu\text{m}$ )	$S_q$ ( $\mu\text{m}$ )	$S_{sk}$	$S_{ku}$		
P-ECO	9.7 ± 1.0	12.4 ± 1.3	9.6 ± 0.6	13.3 ± 0.1	- 1.0 ± 0.7	4.3 ± 1.3	49.3 ± 7.2	38.8 ± 5.8
P-ECO pre-polished	2.7 ± 0.2	3.4 ± 0.2	1.9 ± 0.2	3.1 ± 0.2	- 1.2 ± 1.8	11.4 ± 4.8	42.2 ± 4.5	64.3 ± 3.3
P-PEO	9.9 ± 1.5	13.2 ± 2.1	-	-	-	-	28.4 ± 8.9	25.9 ± 1.5
M-ECO	18.2 ± 9.0	24.5 ± 11.6	10.4 ± 1.63	13.4 ± 1.4	0.7 ± 0.5	3.2 ± 0.1	54.8 ± 18.9	40.0 ± 4.6
M-ECO pre-polished	2.9 ± 0.2	3.8 ± 0.2	3.2 ± 0.1	5.0 ± 0.6	0.1 ± 0.9	6.0 ± 0.2	48.1 ± 7.8	43.3 ± 6.3
M-PEO	18.8 ± 7.8	25.7 ± 10.6	-	-	-	-	27.1 ± 5.8	28.1 ± 0.4
C-ECO	1.8 ± 0.5	2.4 ± 0.7	1.5 ± 0.1	2.0 ± 0.1	0.03 ± 0.1	3.2 ± 0.4	68.0 ± 5.2	67.2 ± 8.2

**Fig. 4** Secondary electron (SE) images of the free surface morphology (general view on the left, higher magnification details on the right) of ECO and PEO-treated A357 (LPBF samples M and P compared with the sand-cast + HIP + T6 alloy, C)



Representative images and corresponding surface topographies are reported in Figure 1S (reported in section “Supplementary material”), which shows a morphological comparison of ECO-treated surfaces for all the substrates (P, M and C) both in the pre-polished (before anodising) and as-built conditions.

Free surface observation (Fig. 4) showed that all the anodic oxide layers were characterised by the typical volcano-like features (due to ejection of molten material from the micro-arc discharge channels), with craters and pores size depending upon both the type of process and the initial roughness of the substrate.



As regards the influence of the type of surface treatment, the higher discharge intensity of PEO produced a lower number of larger crater-like features and pores corresponding to channel entrance than ECO, hence leading to higher surface roughness (Table 6). Regarding the influence of the original substrate roughness on ECO surface morphologies, the comparison of P, M and C showed that the smoother C substrate resulted in an oxide layer with a finer, less porous and denser surface morphology. This led to a smoother and more homogeneous surface quality, as previously discussed. Similar considerations can be drawn also comparing the ECO-treated LPBF samples with pre-polishing before anodising (Fig. 1S).

### 3.2.2 Microstructure and phase composition

Polished cross-sections of anodic oxides are compared in Figs. 5 and 6: all the ECO coatings showed a higher thickness (i.e., Table 6) and denser morphology than those produced by PEO, as previously observed on the wrought AA6082 alloy [13]. This was due to the lower discharge intensity in ECO, which did not lead to extensive ejection of molten material as well as gas evolution from micro-arc discharge channels, typically occurring during PEO [34]. Even though ECO layers were denser than PEO ones, they were characterised by a fine network of channels, with small pores, voids, and cracks, which increased with increasing roughness of the LPBF substrate. A similar correlation between substrate surface roughness and anodic oxide compactness (i.e., the smoother and denser the substrate surface,

the better the coating quality) was observed also by other authors dealing with high-voltage oxidation of non-ferrous alloys, either produced by additive manufacturing (LPBF) [14] or by conventional methods [35]. According to their findings, the detrimental influence of substrate roughness on anodic oxide compactness was attributed to the higher spherical radius of the gas bubbles generated during the anodising process, whose breakdown generated the observed cavities. Microstructural defects and local decreases in the oxides thickness can also be related to the presence of Si-rich region, as also reported for A356 [5] or A359 [36]. This was particularly evident by comparing the ECO layers. In fact, in the case of C-ECO (Fig. 6, bottom row), a slight decrease of oxide thickness was observed over the eutectic Si regions, whilst in P-ECO and M-ECO, only a slight waviness of the substrate–coating interface was observed (Figs. 5 and 6, top rows). In case of LPBF samples, the size of Si-rich constituents was much smaller and more finely distributed than for the C alloy; therefore, this waviness was probably related to the evolution of the anodising process on the rough surface of additively manufactured substrates. This assumption was also supported by the slight waviness reduction observed in P samples after the pre-polishing procedure (Fig. 5), indicating that the shape of the substrate–coating interface was influenced by the topography of the substrate. This effect was less noticeable in M samples, which were rougher than P ones in the as-built conditions and hence benefitted less from pre-polishing, since pre-polishing was carried out using the same procedure for both the LPBF samples.

**Fig. 5** FEG-SEM cross-section images (backscattered electrons) of anodic oxides on LPBF A357 comparing PEO and ECO layers and showing the influence of pre-polishing on the morphology of ECO layers

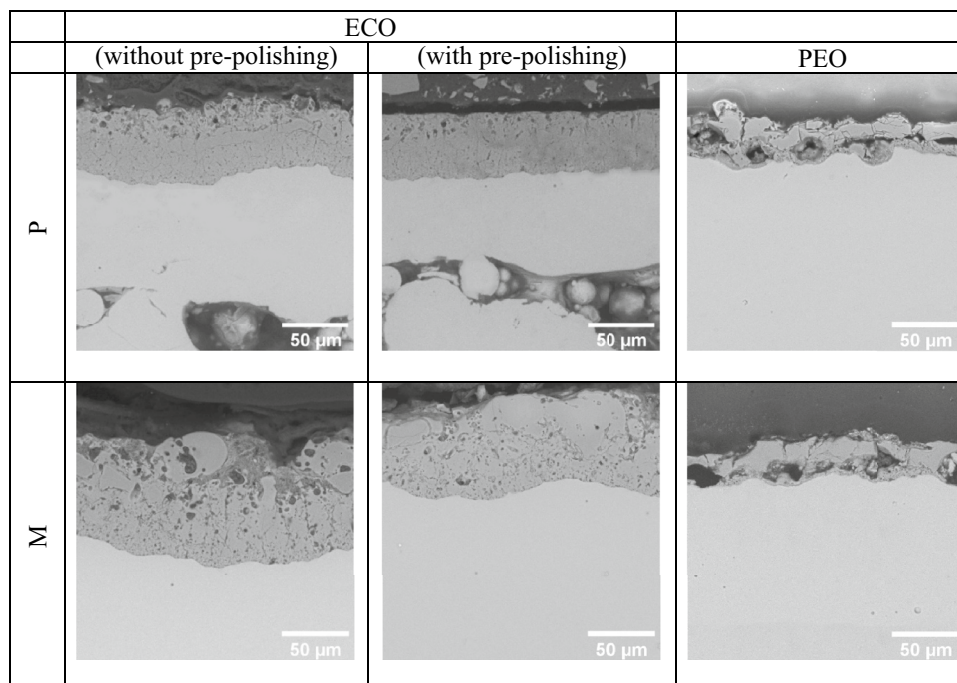
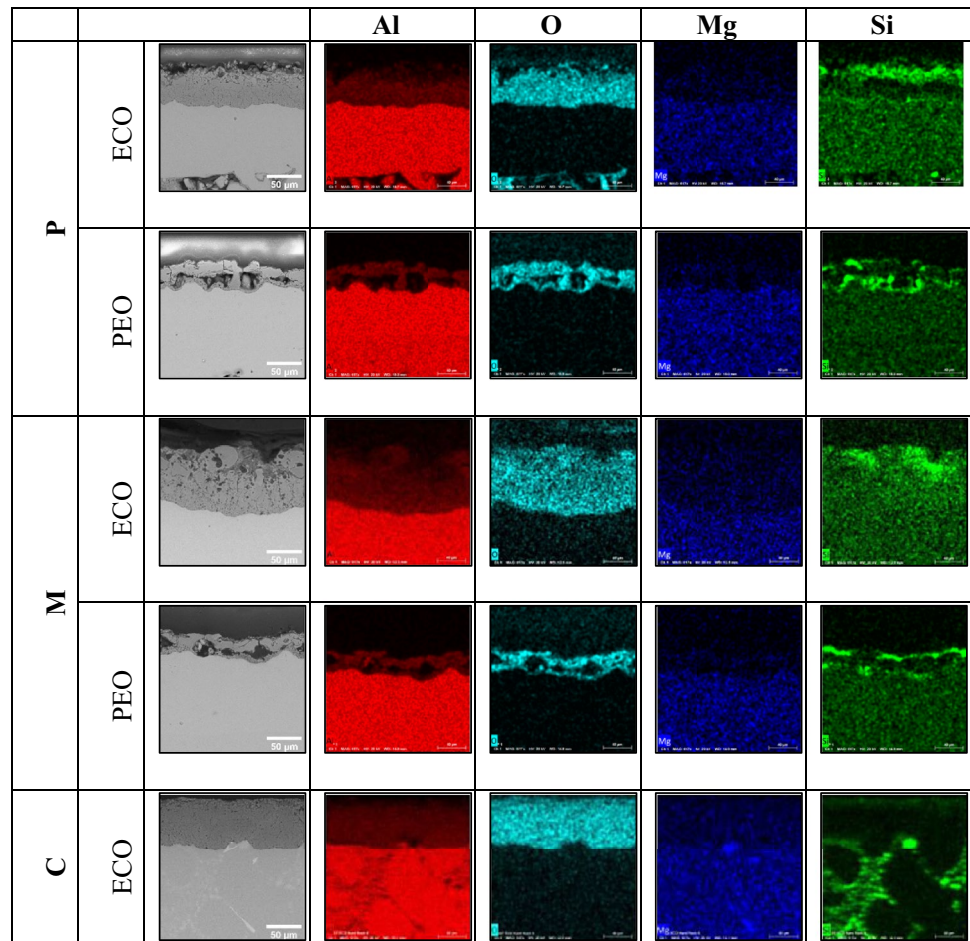


**Fig. 6** EDS X-ray maps of polished cross-sections of LPBF (M, P) and cast (C) A357, anodised by ECO and PEO processes



The ECO layer grown on the smooth C alloy showed a high density and the highest thickness. The lower thickness of P-ECO and M-ECO was probably related to the reduced anodising efficiency in additively manufactured AlSi alloy, attributed by Revilla et al. [7] to the more extensive involvement of the finer Si microconstituents in the oxidation process due to their more favourable surface-to-volume ratio.

Elements distribution along the cross-sections is shown by EDS X-ray maps in Fig. 6. Al and O elements were homogeneously distributed throughout the layers formed on all substrates, suggesting the formation of  $\text{Al}_2\text{O}_3$  as the main phase in all the layers. The distribution of Al and O also further highlighted the higher compactness of ECO layers by comparison to PEO ones. By observing the substrates below the oxide layers, it is possible to confirm that the LPBF process produced a more homogeneous and finer distribution of Si and Mg by comparison to cast A357. This led to the previously mentioned more extensive involvement of Si in the oxidation process occurring during the ECO treatment of LPBF samples by comparison to cast ones, as demonstrated by the detection of Si in P- and M-ECO and its absence from the C-ECO.

Further details highlighted by EDS X-ray maps are reported in Fig. 7, which shows that ECO was able to compensate both surface and surface-connected defects (i.e., spatters and lack of fusion at the contour layer edge, such as those depicted in Fig. 2a, b). As these detrimental features are not sealable by HIP [37], this outcome is very interesting. In fact, the electrolyte was able to enter surface-connected cavities and the anodic oxide sealed them by growing towards the center of the cavity, as shown by the EDS X-ray maps in Fig. 7a and the corresponding scheme in Fig. 8a. A similar phenomenon was also reported by Revilla et al. for HA of different LPBF-fabricated hypoeutectic AlSi alloys [8], as well as by Sabatini et al. [36] for PEO of cast A359 with shrinkage cavities.

Moreover, ECO process also led to an “incorporation” of typical LPBF surface defects such as balling and spatters (Figs. 7b and 8b) in the growing oxide. This phenomenon can be responsible for the low increase in roughness of LPBF samples before and after the anodising process which was discussed when commenting data in Table 6. In fact, a sort of levelling effect occurred when the coating thickness exceeded the size of defects.

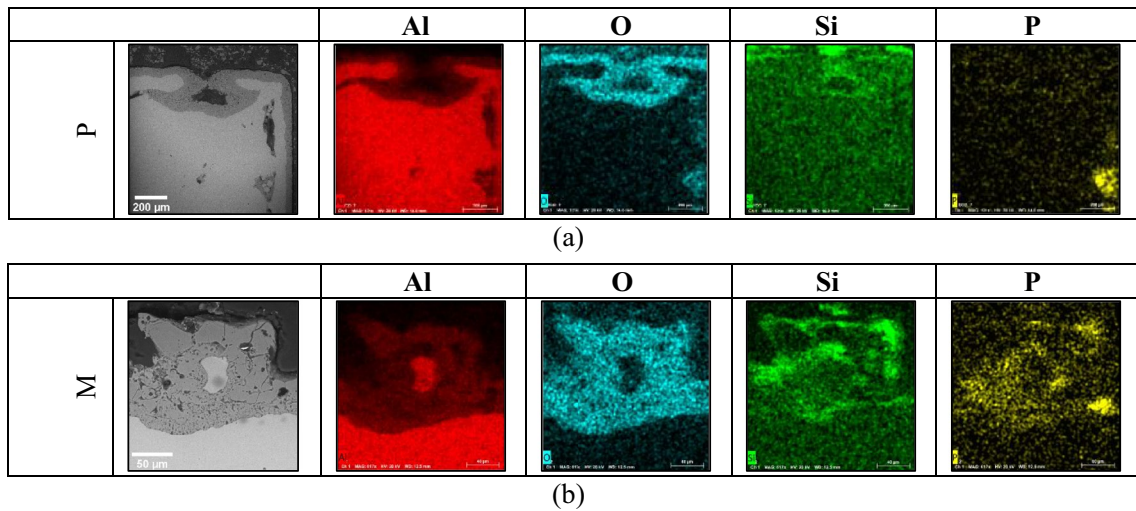


**Fig. 7** EDS X-ray maps showing how the anodic oxide produced by ECO grew on typical defects of LPBF-produced A357: (a) partial sealing of sub-surface cavities: the smaller cavity (bottom right) was

completely filled up by the growing oxide, whilst the bigger one (top centre) was still partly open; (b) oxide growth around a protruding spatter

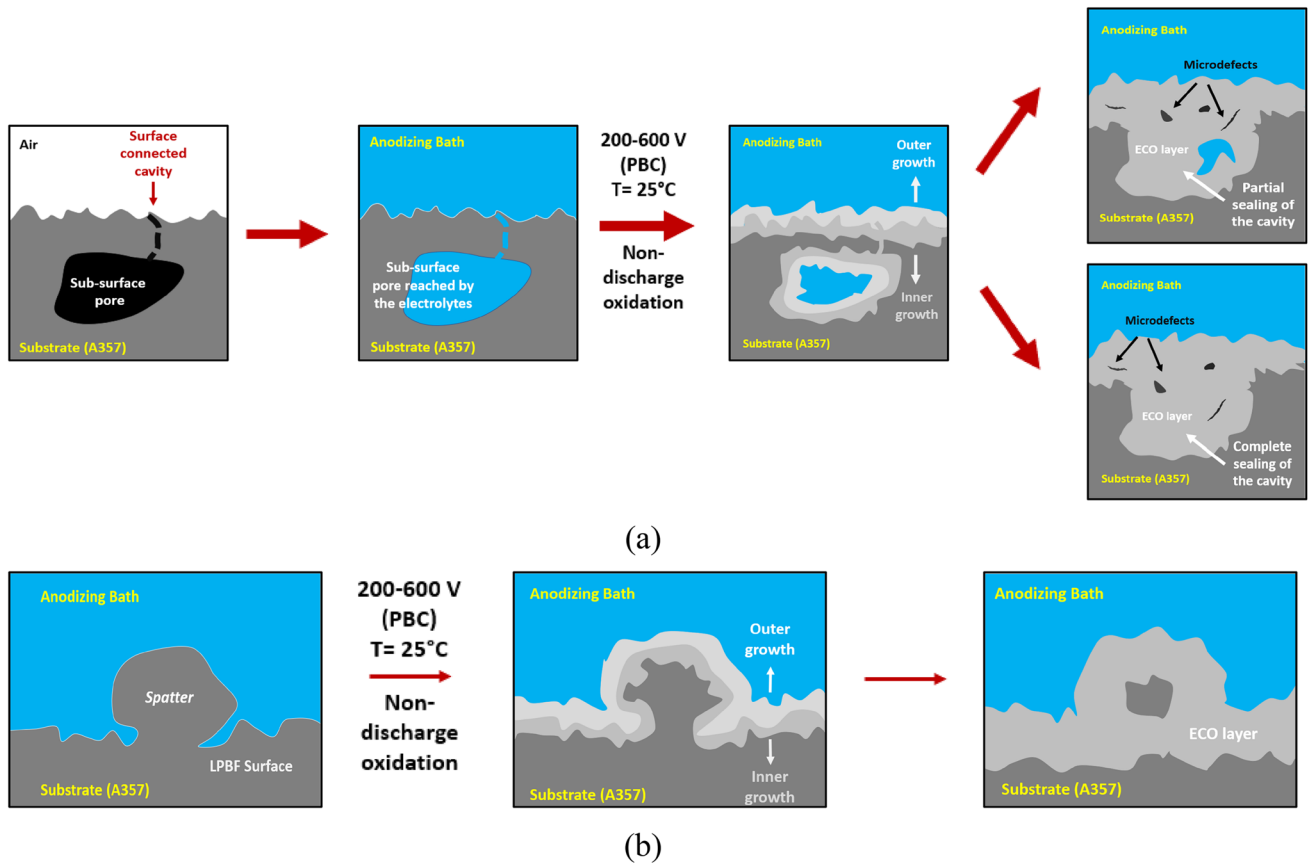


**Fig. 8** Defect compensation mechanisms induced by the growth of anodic oxide on LPBF-fabricated A357: (a) sealing of surface-connected cavities and (b) partial levelling of spatters

**Fig. 9** Indexed  $\theta$ - $2\theta$  X-ray diffraction patterns, representative of the through thickness phase constitution of anodic layers on A357

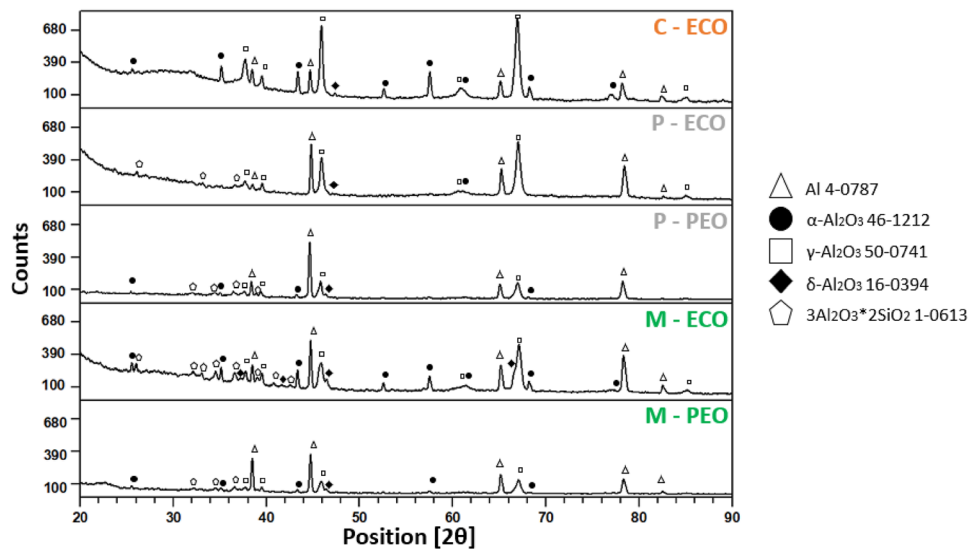


**Table 7** Ratio between integrated diffraction intensities between the (113) peak ( $2\theta=43.4^\circ$ ) of  $\alpha$ - $\text{Al}_2\text{O}_3$  ( $I_\alpha$ ) and the (400) peak ( $2\theta=45.7^\circ$ ) of  $\gamma$ - $\text{Al}_2\text{O}_3$  ( $I_\gamma$ ) for the anodic oxides on A357 [22, 23]

	$I_\alpha/I_\gamma$
P-ECO	0.00
P-PEO	0.17
M-ECO	0.33
M-PEO	0.17
C-ECO	0.18

XRD patterns, representative of the whole layer thickness (as indicated by the detection of substrate peaks), are reported in Fig. 9.

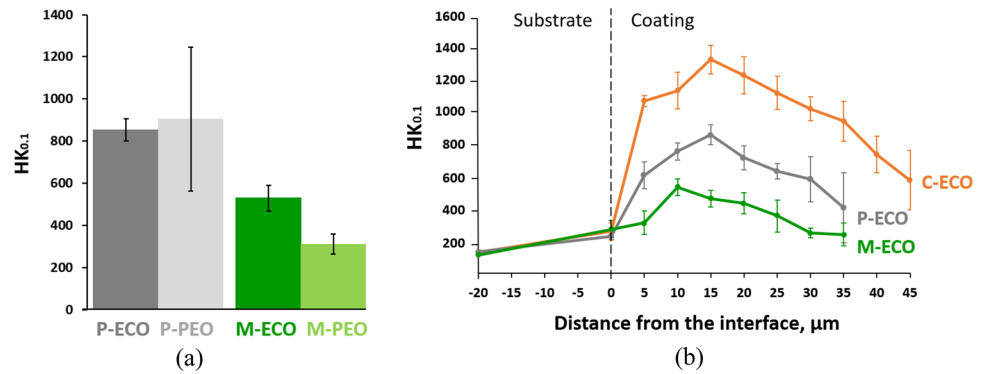
For all ECO and PEO layers, the main crystalline phase was  $\gamma$ - $\text{Al}_2\text{O}_3$ , and also, traces of  $\delta$ - $\text{Al}_2\text{O}_3$  have been detected in all samples, mostly in P-ECO and M-ECO, indicating a partial conversion of  $\gamma$  to  $\alpha$ , in agreement with the  $\gamma \rightarrow \delta \rightarrow \theta \rightarrow \alpha$  sequence [38, 39]. Other detected phases, according to the different oxide layers, were  $\alpha$ - $\text{Al}_2\text{O}_3$  and mullite ( $3\text{Al}_2\text{O}_3 \cdot 2\text{SiO}_2$ ).  $\alpha$ - $\text{Al}_2\text{O}_3$  was found in both P-PEO and M-PEO, that showed also a comparable ratio between  $\alpha$ - and  $\gamma$ - $\text{Al}_2\text{O}_3$  ( $I_\alpha/I_\gamma=0.17$  for both P and M samples, Table 7). A significant amount of  $\alpha$ - $\text{Al}_2\text{O}_3$  was detected also in M-ECO samples ( $I_\alpha/I_\gamma=0.33$ , Table 7), whilst in P-ECO,  $\alpha$ - $\text{Al}_2\text{O}_3$  was not detectable. The detection of  $\alpha$ - $\text{Al}_2\text{O}_3$  in layers obtained by high-voltage anodising has been recently correlated to the predominance of a “soft regime” (as opposed to a more intense and detrimental “arcs regime”), where a significant part of heat remains confined within the coating rather than in the electrolyte, promoting the gradual transformation of metastable phases into the thermodynamically stable  $\alpha$ - $\text{Al}_2\text{O}_3$  [40]. Also, other authors associated the intensification of  $\gamma$ -to- $\alpha$  transition to the soft sparking mode, even though they claimed that it cannot be explained only by thermal activation [41]. Hence, the lower amount of  $\alpha$ - $\text{Al}_2\text{O}_3$  observed in PEO than in ECO layers

might be due to the more intense (i.e., less “soft”) discharge regime. Similarly, when comparing the ECO layers on P and M substrates, the higher amount of  $\alpha$ - $\text{Al}_2\text{O}_3$  in M might be related to the improved microstructure and the absence of sub-surface defects, which may have facilitated the attainment of a “softer” arc regime.

Mullite ( $3\text{Al}_2\text{O}_3 \cdot 2\text{SiO}_2$ ) was detected in ECO and PEO layers grown on LPBF substrates. No trace of mullite was found in C-ECO. Mullite is a stable phase, acting as a thermal barrier, whose formation has been observed several times after PEO in silicate electrolyte, both on wrought AA6082 [42, 43] and on cast alloys as AlSi12 [15] and A356 [5] due to the high temperature ( $> 1400^\circ\text{C}$ ) locally achieved during coating growth. The formation of other Al-Si-O compounds, like kyanite ( $\text{Al}_2\text{SiO}_5$ ), was found in the PEO layer grown on Al-Si alloys both LPBF [14] and cast [15]. In the present study, the formation of mullite is most likely related to the fine and homogeneous distribution of the eutectic Si in LPBF substrates, that, as previously discussed, was involved in the oxidation process. In fact, all the works dealing with anodising of LPBF Al-Si alloys [7, 8, 14, 15] reported that the finer and more homogeneous microstructure of additively manufactured alloys promoted simultaneous oxidation of Al and Si and led to more extensive involvement of Si in the process by comparison to the corresponding cast alloys.

Finally, a broad peak at low  $2\theta$ -angle, related to amorphous constituents, was detected in all ECO layers, whilst it was observed to a lesser extent in PEO. This was probably due to the less-intense discharge regime in ECO, limiting the amorphous-to-crystalline transformations which occurred during coating growth.

**Fig. 10** (a) Comparison of surface micro-hardness of ECO and PEO layers on LPBF A357. (b) Cross-sectional Knoop indentation profiles of ECO coatings on A357



### 3.2.3 Micro-hardness and scratch resistance

Results of micro-hardness measurements ( $HK_{0.1}$ ) performed on the oxide layers are reported in Fig. 10.

Due to the relatively low compactness of PEO layers (Fig. 5), the comparison between ECO and PEO layers grown on LPBF substrates was carried out by measuring the  $HK_{0.1}$  hardness in the denser inner layer for each type of coating (Fig. 10a). On the M substrates, PEO displayed a lower micro-hardness than ECO, whilst this difference was not observed for P substrates, where both PEO and ECO layers showed comparable values. Nonetheless, the micro-hardness of P-PEO displayed a higher standard deviation than P-ECO, due to the lower compactness of PEO.

As ECO layers were generally dense and compact, the oxides grown on the different substrates are compared by showing the micro-hardness profiles performed on the polished cross-section (Fig. 10b). No differences were observed between micro-hardness profiles of ECO layers grown on pre-polished and unpolished substrates and, therefore, only data for unpolished substrates were reported for clarity. By moving from the substrate to the oxide layer, micro-hardness increased with increasing distance from the substrate–coating interface and displayed the highest values at about 1/5 of the coating thickness, in the denser inner layer. Then, it decreased due to the increasing defect density in the outer layer.

C-ECO was characterised by the highest micro-hardness, due to the lower defect density of the coating grown on the smooth C substrate. P-ECO displayed intermediate micro-hardness values, whilst M-ECO showed the lowest values, as also observed by results in Fig. 10b. These outcomes correlate better with defect density observed in cross-section (Fig. 5) than with  $I\alpha/I\gamma$  determined by XRD, indicating that hardness was more beneficially affected by the compactness of the layers than by the amount of hard  $\alpha$ - $Al_2O_3$ .

It should be noticed that all the anodic layers led to an increase in the hardness by comparison to the substrate.

Scratch tests were carried out using critical load for total coating breakthrough ( $L_{c3}$ ) as the main parameter for the

comparison of anodic layers scratch resistance (Table 6). In this work, complete adhesive failure was never observed and the substrate was revealed solely by perforation of the coating after repeated cohesive failure by chipping and/or compressive spallation, as already reported also by Wheeler et al. [44] for PEO layers grown on wrought AA5052 from a silicate-based electrolyte. Therefore,  $L_{c3}$  can be considered here as a measure of coating cohesive strength rather than a measure of practical adhesion.

The ECO layers grown on unpolished LPBF samples showed comparable  $L_{c3}$  values (about 40 N), lower than those obtained on the C alloy, due to their lower thickness, hardness, compactness, and higher surface roughness.

Pre-polishing before ECO beneficially affected the anodic layers on P, but it did not significantly affect the scratch behaviour of the layers on M. In fact, ECO layers on P reached  $L_{c3}$  values comparable to those obtained on the C alloy. As already mentioned, when discussing the polished cross-sections in Fig. 5, M samples were rougher than P ones in the as-built conditions (Table 6) and hence benefited less from pre-polishing, achieving a less compact morphology which detrimentally affected also scratch resistance.

All the ECO layers showed higher  $L_{c3}$  than PEO, due to both their lower defect density and higher thickness (which is known to significantly affect scratch performance of PEO layers [39, 44]).

### 3.3 Dry sliding tests

Tribological behaviour was analysed on the basis of the steady-state values of the coefficient of friction (COF) in Fig. 11, the maximum wear depths (WDs) measured on sliders at the end of tests in Fig. 12, and the morphology of worn surfaces observed by SEM in Fig. 13. Results are firstly discussed by comparing the effect of PEO and ECO treatment applied on the LPBF substrates, and then by focusing on the influence of the substrate on the behaviour of the ECO layers.

**Fig. 11** Dry sliding tests, average steady-state coefficient of friction (COF) vs normal load: (a) comparison of PEO and ECO on LPBF-A357 at 20 N; (b) influence of the ECO treatment (without pre-polishing) on LPBF and cast A357; (c) influence of pre-polishing on ECO-treated LPBF-A357

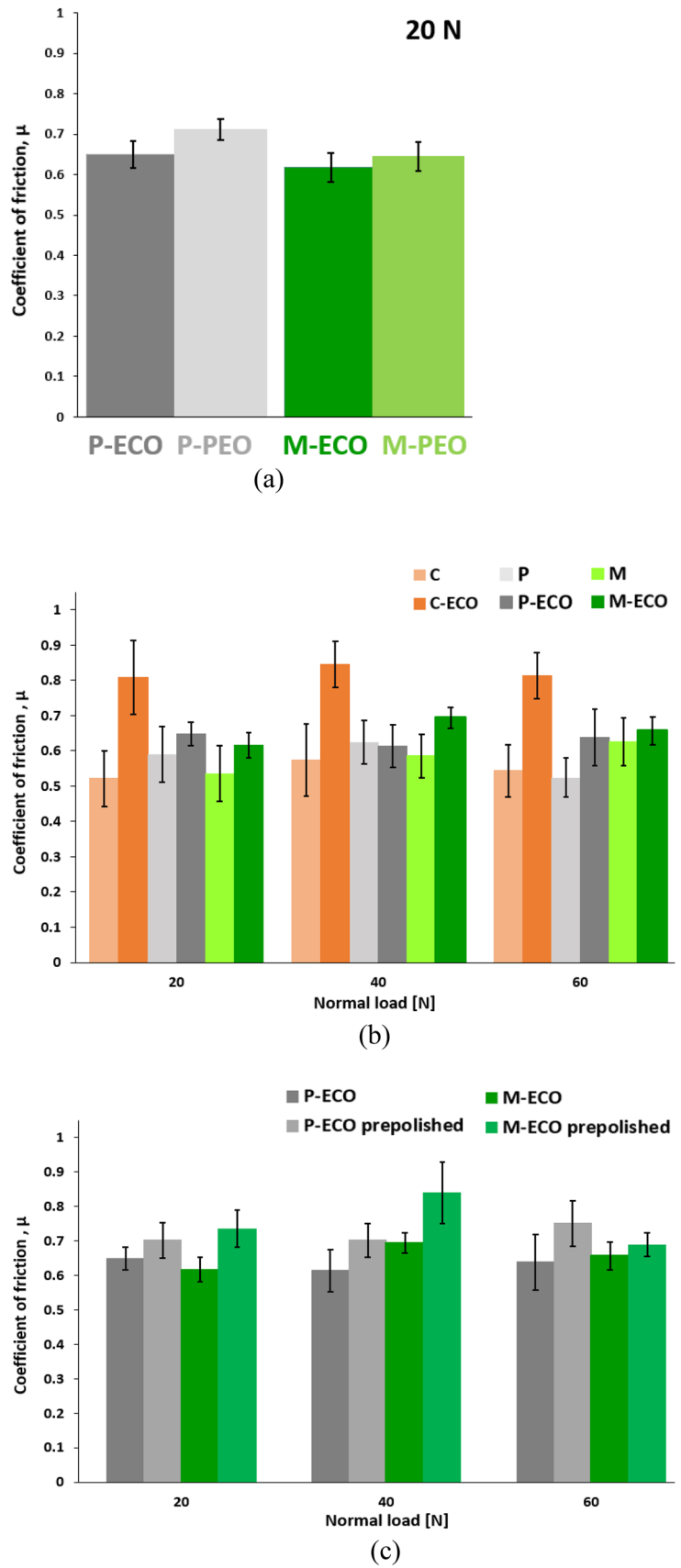
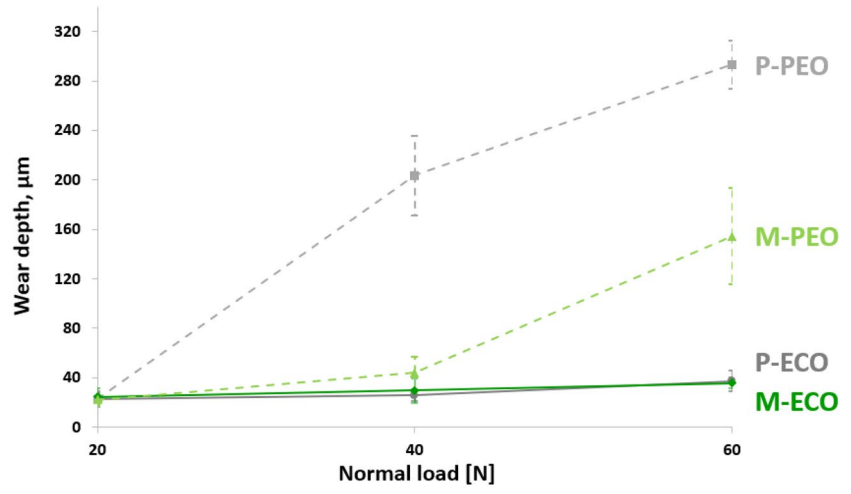
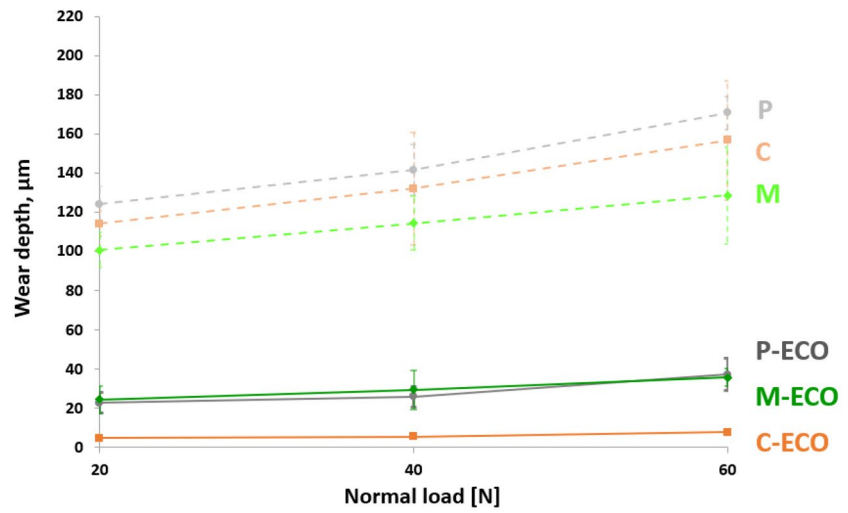


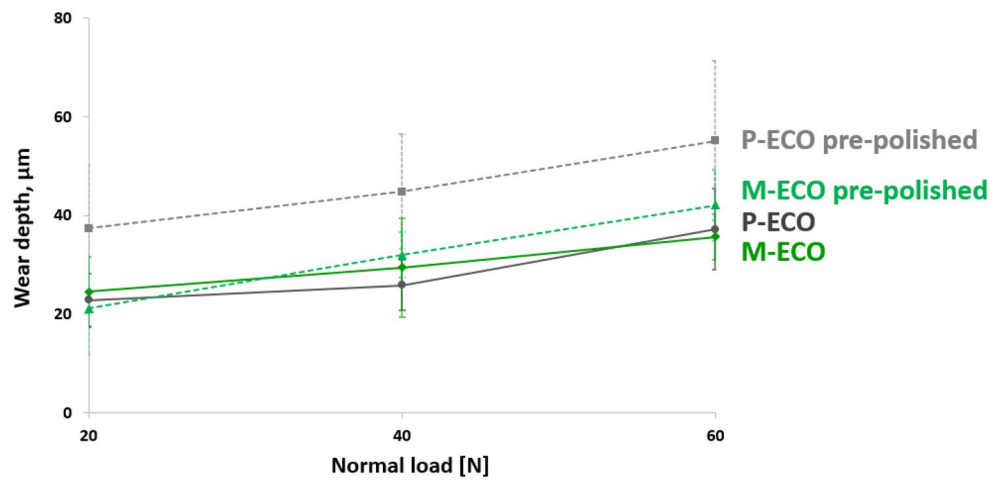
**Fig. 12** Dry sliding tests: maximum wear depth (WD) vs normal load: (a) comparison of PEO and ECO on LPBF-A357; (b) influence of the ECO treatment (without pre-polishing) on LPBF and cast A357; (c) influence of pre-polishing on ECO-treated LPBF-A357



(a)

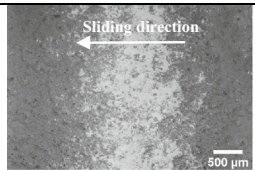
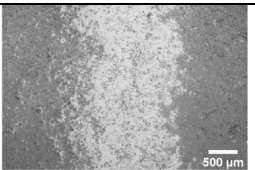
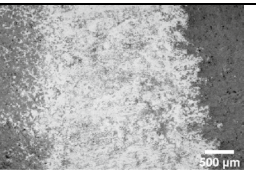
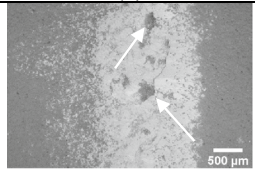
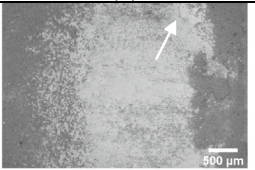
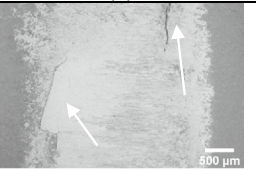
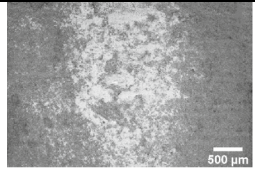
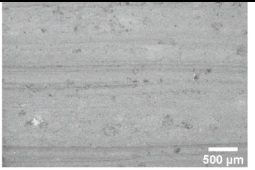
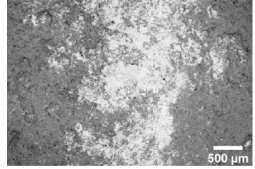
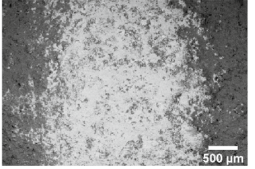
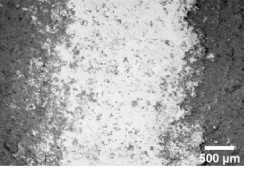
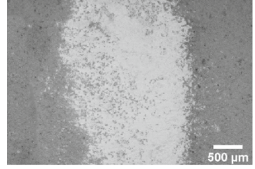
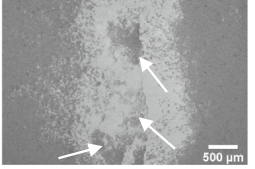
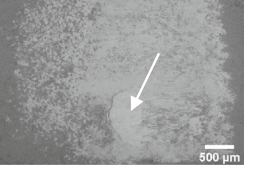
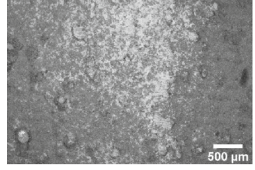
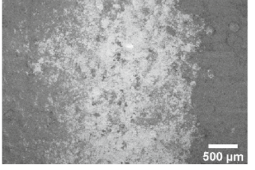
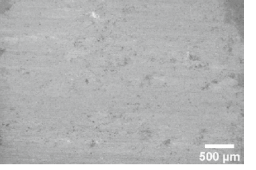
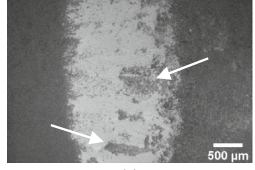
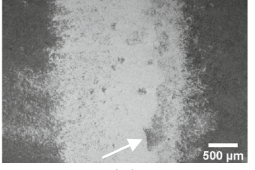
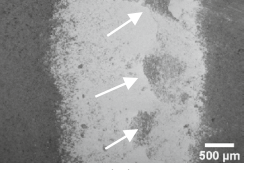


(b)



(c)

**Fig. 13** Dry sliding tests: back-scattered electron images of wear scars on anodised A357. White arrows indicated transfer layer delamination areas

	20 N	40 N	60 N
P-ECO	 (a)	 (b)	 (c)
P-ECO pre-polished	 (d)	 (e)	 (f)
P-PEO	 (g)	 (h)	(n.a.) Coating failed at 40 N
M-ECO	 (i)	 (l)	 (m)
M-ECO pre-polished	 (n)	 (o)	 (p)
M-PEO	 (q)	 (r)	 (s)
C-ECO	 (t)	 (u)	 (v)

### 3.3.1 PEO and ECO layers on LPBF substrates

Figure 11 compares the frictional and wear behaviour of ECO and PEO layers on LPBF substrates. For the steady-state COF (Fig. 11a), solely data measured at 20 N were reported, because at higher loads, PEO layers were completely worn out before the end of the test (at 40 N for P-PEO and 60 N for M-PEO), as also demonstrated by the

increasing WDs in Fig. 12a. PEO layers generally showed slightly higher COF values than ECO, probably due to extensive micro-fragmentation (promoted by the higher defect density of PEO, as shown by cross-sections in Fig. 5), leading to the formation of hard particles at the contact interface and to the subsequent increase of the abrasive component of friction. PEO layers failed during the test, leading to involvement of the bare substrate in the contact and to the



consequent remarkable increase of WD (Fig. 12a). Extensive ploughing of the substrate occurred after the PEO layer was completely worn out, due to the hard abrasive particles from the layer itself, as shown by SEM images in Fig. 13h (P-PEO) and 13s (M-PEO), taken after tests which induced complete coating failure. Conversely, ECO layers never underwent complete failure and they succeeded in increasing the wear resistance by comparison to the untreated alloy (Fig. 12b). On the other hand, when the PEO layer was completely worn out, the measured WDs were comparable and even higher than the untreated alloy tested in the same condition. It is worth noting that the slightly thicker and “softer” PEO layer on M failed at a higher normal load than the harder (and hence probably more brittle, or less strain-tolerant) PEO layer on P.

### 3.3.2 ECO layers on LPBF substrates

By focusing on the frictional behaviour of ECO layers (Fig. 11b), it can be noticed that normal load did not significantly affect COF in the investigated load range. With the sole exception of P-ECO at 40 N, ECO samples, as well as PEO ones, showed higher COFs than the untreated P, M, and C samples. This is due to the typical increase in the abrasive component of friction induced by the hard and rough anodised surface [13]. This effect was particularly pronounced in the case of C-ECO, which showed the highest  $HK_{0.1}$  values (Fig. 10b). The lower COFs of P-ECO and M-ECO alloys can be related to a lower abrasive component due to their lower hardness. However, it can be also related to the higher stability of an iron-oxide-based transfer layer formed on worn surfaces due to mild tribo-oxidation of the steel counterface, induced by the combined action of contact stresses and frictional heating [36]. The presence of such layer was proved by SEM analyses of wear scars (Figs. 13a–c and i–m), where it appears as a light-grey powdery layer covering the wear scars, as also further demonstrated by localised EDS analyses reported in the supplementary material (Fig. 2S). This transfer layer was more stable on the surface of P-ECO and M-ECO, due to their

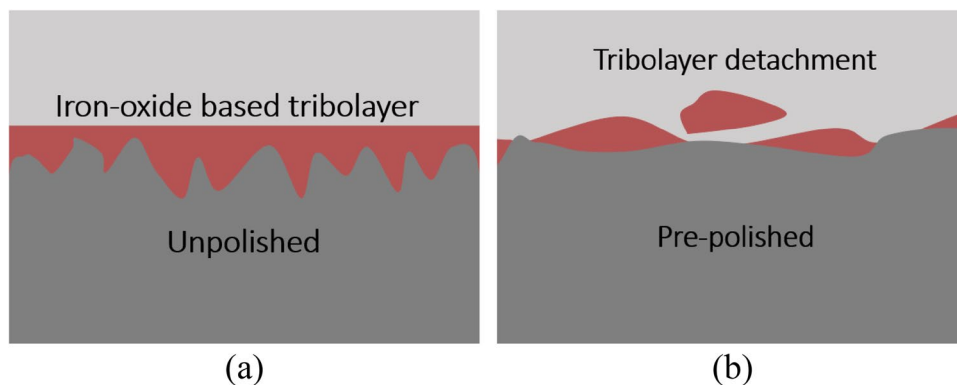
higher surface roughness, than on C-ECO (Table 6), promoting the entrapment of wear debris [45]. The formation of this transfer layer was generally ascribed to tribo-oxidation of the steel counterpart.

The effect of pre-polishing of LPBF surfaces is shown in Fig. 11c. Generally, pre-polishing led to higher COF values, possibly as a consequence of the lower stability of the oxide-based transfer layer. Even though the pre-polishing of the LPBF substrate resulted in denser ECO layers, with higher cohesive strength (as discussed in Sect. 3.2), the lower surface roughness (Table 6) detrimentally affected the retention of the iron-oxide-based transfer layer on the worn surface, hence leading to higher COFs. In fact, on the smoother surfaces, the iron-oxide transfer layer probably achieved more easily the critical thickness for delamination [46]. This assumption was evidenced by worn surfaces where transfer layer delamination was more frequently observed on pre-polished samples (as indicated by arrows in Fig. 13d–f and n–p). Further evidence on the delamination tendency of the transfer layer was found by analysing worn surfaces of C-ECO, characterised by the lowest surface roughness. A schematic representation of the effect of surface roughness on the stability of such protective oxide layer is depicted in Fig. 14.

C-ECO showed the highest wear resistance, thanks to the higher thickness, compactness, and hardness, even though the lower surface roughness detrimentally affected the stability of the above discussed Fe–O transfer layer.

The comparison of P-ECO and M-ECO (Fig. 12b) showed that, even though the P substrate displayed significant subsurface defects at the contour layer edge (Fig. 2), the ability of the ECO treatment to compensate them (Figs. 7 and 8) allowed to obtain comparable WDs for anodic layer grown on both substrates, which also displayed comparable cohesive strength ( $L_{c3}$  in Table 6) and thickness. As regards the influence of pre-polishing (Fig. 12c), ECO layers grown on unpolished LPBF substrates showed a slightly higher wear resistance than those on pre-polished ones, probably because of the higher stability of the protective Fe–O transfer layer on their rougher surface, even though the layer grown on

**Fig. 14** Schematic showing the influence of pre-polishing before ECO (inducing a lower anodic oxide roughness) on the stability of the iron-oxide-based tribolayer: (a) unpolished or (b) pre-polished LPBF substrates



unpolished substrates was less dense and more defective than those grown on pre-polished ones. Therefore, the stability of the Fe–O transfer layer seems to be the dominant factor affecting the dry sliding wear behaviour of the anodised A357 in the investigated conditions.

## 4 Conclusions

The dry sliding behaviour of LPBF as-built A357 aluminium alloy, anodised both by Electrochemical Oxidation (ECO) and by Plasma Electrolytic Oxidation (PEO), was investigated and related to microstructural and micro-mechanical features. As regards ECO, the influence of two sets of LPBF-process parameters (i.e., maximised productivity, P, or improved microstructure, M) was investigated, as well as the influence of polishing the as-built LPBF substrate before anodising. The ECO-treated A357 sand-cast alloy (subjected to hot-isostatic pressing and T6 heat treatment, C) was used as benchmark. The following conclusions can be drawn from this work:

- LPBF samples showed a hierarchical microstructure with micrometric melt pools and a very fine cellular solidification sub-structure, consisting of sub-micrometric primary Al cells surrounded by a network of very fine eutectic Si. M samples showed a more homogeneous and less porous microstructure than P ones, with no porosity underneath the edge of the layer.
- The ECO treatment allowed to produce quite homogeneous anodic oxides both on C and on LPBF A357. ECO coating compensated superficial and surface-connected defects of LPBF samples, inducing a lower roughness increase than C alloy.
- ECO layers on the C alloy showed the highest dry sliding wear resistance, since they were characterised by higher thickness, cohesion, and micro-hardness, even though they revealed the highest coefficient of friction (COF) in all the tested conditions. In fact, the rougher surface of ECO layers on LPBF substrates led to a higher stability of the iron-oxide transfer layer (deriving from tribo-oxidation of the steel counterface), beneficially affecting friction behaviour.
- Pre-polishing of LPBF led to thinner but denser and smoother ECO layers, with a high cohesive strength. However, the decreased stability of the iron-oxide transfer layer on the smoother surface of these ECO layers led to an increase in the COF values and a slight decrease in the wear resistance. Therefore, it is not advisable to introduce the pre-polishing step in the ECO treatment cycle of LPBF substrates, which may be directly treated in the as-built condition.
- The ECO process produced a thicker, less-defective anodic oxide than PEO, with a higher scratch resistance

(related to cohesive strength), which allowed ECO layers to withstand the sliding tests in the whole load range without being completely worn out. Conversely, PEO layers on LPBF substrates underwent failure before test completion.

**Supplementary Information** The online version contains supplementary material available at <https://doi.org/10.1007/s40964-022-00353-z>.

**Acknowledgements** The research work carried out by Luca Lorenzetti was funded by “POR/FSE 2014/2020: Alte Competenze per la Ricerca e il Trasferimento Tecnologico” under Grant No. 2019-11458-RER. The authors would like to acknowledge Dr. Erica Liverani and Dr. Giuseppe Valli of the Laser Group of the Industrial Engineering Department of the University of Bologna, led by Prof. Fortunato, for their invaluable support in LPBF printing of the substrates.

**Funding** Open access funding provided by Alma Mater Studiorum - Università di Bologna within the CRUI-CARE Agreement.

**Open Access** This article is licensed under a Creative Commons Attribution 4.0 International License, which permits use, sharing, adaptation, distribution and reproduction in any medium or format, as long as you give appropriate credit to the original author(s) and the source, provide a link to the Creative Commons licence, and indicate if changes were made. The images or other third party material in this article are included in the article's Creative Commons licence, unless indicated otherwise in a credit line to the material. If material is not included in the article's Creative Commons licence and your intended use is not permitted by statutory regulation or exceeds the permitted use, you will need to obtain permission directly from the copyright holder. To view a copy of this licence, visit <http://creativecommons.org/licenses/by/4.0/>.

## References

1. Ceschini L, Toschi S (2017) Friction and wear of aluminum alloys and composites. In: Friction, lubrication, and wear technology, vol 18. ASM Handbook, ASM International, pp 509–532. <https://doi.org/10.31399/asm.hb.v18.a0006388>
2. Aboulkhair NT, Simonelli M, Parry L, Ashcroft I, Tuck C, Hague R (2019) 3D printing of aluminium alloys: additive manufacturing of aluminium alloys using selective laser melting. *Prog Mater Sci* 106:100578. <https://doi.org/10.1016/j.pmatsci.2019.100578>
3. Casati R, Vedani M (2019) Aging response of an A357 Al alloy processed by selective laser melting. *Adv Eng Mater* 21:1–7. <https://doi.org/10.1002/adem.201800406>
4. Fratila-Apachitei LE, Tichelaar FD, Thompson GE et al (2004) A transmission electron microscopy study of hard anodic oxide layers on AlSi(Cu) alloys. *Electrochim Acta* 49:3169–3177. <https://doi.org/10.1016/j.electacta.2004.02.030>
5. Mohedano M, Matykina E, Arrabal R, Mingo B, Pardo A (2015) PEO of pre-anodized Al-Si alloys: corrosion properties and influence of sealings. *Appl Surf Sci* 346:57–67. <https://doi.org/10.1016/j.apsusc.2015.03.206>
6. Zhu B, Seifeddine S, Persson POÅ, Jarfors AEW, Leisner P, Zanella C (2016) A study of formation and growth of the anodised surface layer on cast Al-Si alloys based on different analytical techniques. *Mater Des* 101:254–262. <https://doi.org/10.1016/j.matdes.2016.04.013>

7. Revilla RI, Terryn H, De Graeve I (2018) Role of Si in the anodizing behavior of Al-Si alloys: additive manufactured and cast Al-Si10-Mg. *J Electrochem Soc* 165:C532–C541. <https://doi.org/10.1149/2.1301809jes>
8. Revilla RI, Rojas Y, De Graeve I (2019) On the impact of Si Content and porosity artifacts on the anodizing behavior of additive manufactured Al-Si alloys. *J Electrochem Soc* 166:C530–C537. <https://doi.org/10.1149/2.1351914jes>
9. Yerokhin AL, Nie X, Leyland A, Matthews A, Doney SJ (1999) Plasma electrolysis for surface engineering. *Surf Coatings Technol* 122:73–93. [https://doi.org/10.1016/S0257-8972\(99\)00441-7](https://doi.org/10.1016/S0257-8972(99)00441-7)
10. Malayoglu U, Tekin KC, Malayoglu U, Shrestha S (2011) An investigation into the mechanical and tribological properties of plasma electrolytic oxidation and hard-anodized coatings on 6082 aluminum alloy. *Mater Sci Eng A* 528:7451–7460. <https://doi.org/10.1016/j.msea.2011.06.032>
11. Jiang BL, Wang YM (2010) 5 - Plasma electrolytic oxidation treatment of aluminium and titanium alloys. In: Dong HBT-SE of LA (ed) Woodhead Publishing Series in Metals and Surface Engineering. Woodhead Publishing, pp 110–154. <https://doi.org/10.1533/9781845699451.2.110>
12. Hussein RO, Northwood DO, Su JF, Nie X (2013) A study of the interactive effects of hybrid current modes on the tribological properties of a PEO (plasma electrolytic oxidation) coated AM60B Mg-alloy. *Surf Coatings Technol* 215:421–430. <https://doi.org/10.1016/j.surfcoat.2012.08.082>
13. Sola R, Tonelli L, Shashkov P, Bogdanoff TH, Martini C (2020) Anodizing of AA6082-T5 by conventional and innovative treatments: microstructural characterization and dry sliding behaviour. *Wear* 458–459:203423. <https://doi.org/10.1016/j.wear.2020.203423>
14. Pezzato L, Dabalà M, Gross S, Brunelli K (2020) Effect of microstructure and porosity of AlSi10Mg alloy produced by selective laser melting on the corrosion properties of plasma electrolytic oxidation coatings. *Surf Coatings Technol* 404:126477. <https://doi.org/10.1016/j.surfcoat.2020.126477>
15. Rogov AB, Lyu H, Matthews A, Yerokhin A (2020) AC plasma electrolytic oxidation of additively manufactured and cast AlSi12 alloys. *Surf Coatings Technol* 399:126116. <https://doi.org/10.1016/j.surfcoat.2020.126116>
16. Carpenter Technology. <https://www.carpenter-technology.com/>. Accessed Dec 2022
17. ASTM B179-18 (2018) Standard specification for aluminum alloys in ingot and molten forms for castings from all casting processes. *ASM International*, pp 1–10. <https://doi.org/10.1520/B0179-18>
18. Tonelli L, Liverani E, Valli G, Fortunato A, Ceschini L (2020) Effects of powders and process parameters on density and hardness of A357 aluminum alloy fabricated by selective laser melting. *Int J Adv Manuf Technol* 106:371–383. <https://doi.org/10.1007/s00170-019-04641-x>
19. International Organization for Standardization (1998) ISO 4288:1998. Geometrical Product Specifications (GPS) - Surface texture: Profile method - Rules and procedures for the assessment of surface texture
20. ASTM B962-17 (2017) Standard Test Methods for Density of Compacted or Sintered Powder Metallurgy (PM) Products Using Archimedes' Principle. *ASM International*, pp 1–7. <https://doi.org/10.1520/B0962-17>
21. Anderson K, Weritz J, Kaufman JG (2019) Properties and selection of aluminum alloys. *ASM Handbook*, vol 2B. *ASM International*, pp 553–555. <https://doi.org/10.31399/asm.hb.v02b.a0006569>
22. Xue W, Deng Z, Lai Y, Chen R (1998) Analysis of phase distribution for ceramic coatings formed by microarc oxidation on aluminum alloy. *J Am Ceram Soc* 81:1365–1368. <https://doi.org/10.1111/j.1151-2916.1998.tb02493.x>
23. Arrabal R, Mohedano M, Matykina E, Pardo A, Mingo B, Merino MC (2015) Characterization and wear behaviour of PEO coatings on 6082-T6 aluminium alloy with incorporated  $\alpha$ -Al<sub>2</sub>O<sub>3</sub> particles. *Surf Coat Technol* 269:64–73. <https://doi.org/10.1016/j.surfcoat.2014.10.048>
24. ASTM G77-17 (2017) Standard test method for ranking resistance of materials to sliding wear using block-on-ring wear test. *ASTM international*, pp 1–11. <https://doi.org/10.1520/G0077-17>
25. Williams JA, Dwyer-Joyce RS (2001) Contact between solid surfaces. In: Bharat B (ed) *Modern tribology handbook*, two volume set, 1st edn. CRC Press, Boca Raton. <https://doi.org/10.1201/9780849377877>
26. Thijs L, Kempen K, Kruth JP, Van Humbeeck J (2013) Fine-structured aluminium products with controllable texture by selective laser melting of pre-alloyed AlSi10Mg powder. *Acta Mater* 61:1809–1819. <https://doi.org/10.1016/j.actamat.2012.11.052>
27. Lorusso M, Trevisan F, Calignano F, Lombardi M, Manfredi D (2020) A357 alloy by lpbf for industry applications. *Materials (Basel)* 13:1–12. <https://doi.org/10.3390/ma13071488>
28. Tonelli L, Liverani E, Morri A, Ceschini L (2021) Role of direct aging and solution treatment on hardness, microstructure and residual stress of the A357 (AlSi7Mg0.6) alloy produced by powder bed fusion. *Metall Mater Trans B* 52:2484–2496. <https://doi.org/10.1007/s11663-021-02179-6>
29. Liu X, Zhao C, Zhou X, Shen Z, Liu W (2019) Microstructure of selective laser melted AlSi10Mg alloy. *Mater Des* 168:107677. <https://doi.org/10.1016/j.matdes.2019.107677>
30. Kimura T, Nakamoto T (2016) Microstructures and mechanical properties of A356 (AlSi7Mg0.3) aluminum alloy fabricated by selective laser melting. *Mater Des* 89:1294–1301. <https://doi.org/10.1016/j.matdes.2015.10.065>
31. Aboulkhair NT, Everitt NM, Maskery I, Ashcroft I, Tuck C (2017) Selective laser melting of aluminum alloys. *MRS Bull* 42:311–319. <https://doi.org/10.1557/mrs.2017.63>
32. DebRoy T, Wei HL, Zuback JS, Mukherjee T, Elmer JW, Milewski JO, Beese AM, Wilson-Heid A, De A, Zhang W (2018) Additive manufacturing of metallic components – Process, structure and properties. *Prog Mater Sci* 92:112–224. <https://doi.org/10.1016/j.pmatsci.2017.10.001>
33. Bhushan B (2000) Surface roughness analysis and measurement techniques. In: Bharat B (ed) *Modern tribology handbook*, two volume set, 1st edn. CRC Press, Boca Raton, pp 79–150. <https://doi.org/10.1201/9780849377877>
34. Huang X (2019) Plasma electrolytic oxidation coatings on aluminum alloys: microstructures, properties, and applications. *Mod Concepts Mater Sci*. <https://doi.org/10.33552/mcms.2019.02.000526>
35. Zhu L, Petrova RS, Gashinski JP, Yang Z (2017) The effect of surface roughness on PEO-treated Ti-6Al-4V alloy and corrosion resistance. *Surf Coatings Technol* 325:22–29. <https://doi.org/10.1016/j.surfcoat.2017.05.044>
36. Sabatini G, Ceschini L, Martini C, Williams JA, Hutchings IM (2010) Improving sliding and abrasive wear behaviour of cast A356 and wrought AA7075 aluminium alloys by plasma electrolytic oxidation. *Mater Des* 31:816–828. <https://doi.org/10.1016/j.matdes.2009.07.053>
37. Atkinson HV, Davies S (2000) Fundamental aspects of hot isostatic pressing: An overview. *Metall Mater Trans A* 31:2981–3000. <https://doi.org/10.1007/s11661-000-0078-2>
38. Lamouri S, Hamidouche M, Bouaouadja N, Belhouchet H, Garnier V, Fantozzi G, Trelkat JF (2017) Control of the  $\gamma$ -alumina to  $\alpha$ -alumina phase transformation for an optimized alumina densification. *Bol la Soc Esp Ceram y Vidr* 56:47–54. <https://doi.org/10.1016/j.bsecv.2016.10.001>

39. Nie X, Leyland A, Song HW, Yerokhin AL, Dowey SJ, Matthews A (1999) Thickness effects on the mechanical properties of micro-arc discharge oxide coatings on aluminium alloys. *Surf Coatings Technol* 116–119:1055–1060. [https://doi.org/10.1016/S0257-8972\(99\)00089-4](https://doi.org/10.1016/S0257-8972(99)00089-4)
40. Martin J, Nominé A, Ntomprougkidis V, Migot S, Bruyère S, Soldera F, Belmonte T, Henrion G (2019) Formation of a metastable nanostructured mullite during Plasma Electrolytic Oxidation of aluminium in “ soft ” regime condition. *Mater Des* 180:107977. <https://doi.org/10.1016/j.matdes.2019.107977>
41. Rogov AB, Matthews A, Yerokhin A (2019) Role of cathodic current in plasma electrolytic oxidation of Al : a quantitative approach to in-situ evaluation of cathodically induced effects. *Electrochim Acta* 317:221–231. <https://doi.org/10.1016/j.electacta.2019.05.161>
42. Curran JA, Kalkanci H, Magurova Y, Clyne TW (2007) Mullite-rich plasma electrolytic oxide coatings for thermal barrier applications. *Surf Coatings Technol* 201:8683–8687. <https://doi.org/10.1016/j.surfcoat.2006.06.050>
43. Dehnavi V, Li B, Shoesmith DW, Liu XY, Rohani S (2013) Effect of duty cycle and applied current frequency on plasma electrolytic oxidation (PEO) coating growth behavior. *Surf Coat Technol* 226:100–107. <https://doi.org/10.1016/j.surfcoat.2013.03.041>
44. Wheeler JM, Curran JA, Shrestha S (2012) Microstructure and multi-scale mechanical behavior of hard anodized and plasma electrolytic oxidation (PEO) coatings on aluminum alloy 5052. *Surf Coatings Technol* 207:480–488. <https://doi.org/10.1016/j.surfcoat.2012.07.056>
45. Cotell CM, Sprague JA, Smidt FA (2018) *Surface Engineering: Topography of Surfaces*. ASM Handbook, vol 5. ASM International, pp 136–138. <https://doi.org/10.31399/asm.hb.v05.a0001236>
46. Quinn TFJ (1992) Oxidational wear modelling: I. *Wear* 153:179–200. [https://doi.org/10.1016/0043-1648\(92\)90269-E](https://doi.org/10.1016/0043-1648(92)90269-E)

**Publisher's Note** Springer Nature remains neutral with regard to jurisdictional claims in published maps and institutional affiliations.